www.ietdl.org

Published in IET Microwaves, Antennas & Propagation
Received on 25th December 2013
Revised on 18th August 2014
Accepted on 18th October 2014
doi: 10.1049/iet-map.2013.0714

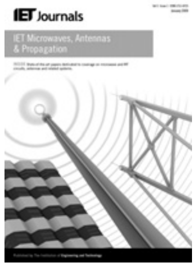

ISSN 1751-8725

Constitutive parameters extraction for thin two-dimensional cylinders based on scattering field measurements

Vladimir Vulfin, Reuven Shavit

Department of Electrical Engineering, Ben-Gurion University of the Negev, Beer Sheva 84105, Israel
E-mail: rshavit@ee.bgu.ac.il

Abstract: This study presents an analytical method for extracting the constitutive parameters of an isotropic two-dimensional magneto-dielectric thin cylinder (small radius compared with the wavelength). The method is based on the scattered far field information to a plane wave illumination. Three variations of the method are presented. First, the complex monostatic scattered fields of two orthogonal polarisations are used to extract the complex constitutive parameters (permittivity and permeability) of a lossy cylinder. Second, the complex bistatic and monostatic scattered fields for a single polarisation are used to extract the complex permittivity and permeability. Third, the absolute value of the monostatic radar cross section for two orthogonal polarisations is used to extract the complex permittivity or permeability. An approximation for a small argument is used to obtain a simple polynomial expression for the scattered field to extract the constitutive parameters. Numerical examples to validate the proposed extraction methods are shown and the results are satisfactory.

1 Introduction

Three major methods of extraction the constitutive parameters of isotropic dielectric and magnetic lossy materials can be found in the literature.

The first method is based on the measured reflection data because of the impedance discontinuity caused by the presence of the unknown material in a transmission line [1–3] or in free space. The transmission line reflection measurements are conducted with the sample in a transmission line ended with short and open loads. In free space, the measurements are conducted using transmit and receive antennas side by side with the sample positioned in front of them. The calibration of the system is performed using a conductive plate.

The second method to extract the constitutive parameters of a sample is based on the transmission measurement data [4–6]. Similarly to the reflection method, the measurements are performed in a transmission line with the sample inserted in the transmission line or in free space with the sample inserted in between the transmit and receive antennas.

The third method is based on the variation of the electrical characteristics of a resonator with and without the sample in the resonator [7–10]. The types of resonators used are: dielectric resonator, coaxial surface wave resonator and split resonator. In the resonator method, the sensitivity and accuracy increases, if the resonator energy is mainly concentrated in the sample.

In this paper, we present a new analytical method for extracting the constitutive parameters of an isotropic two-dimensional (2D) magneto-dielectric thin cylinder (small radius compared with the wavelength), taking advantage of its scattered far field information. This work is based on the work presented in [11] for calculating the scattered fields from a magneto-dielectric cylinder, but goes beyond. It presents three extraction methods for the constitutive parameters in case of 2D thin cylinders.

2 Scattered far field calculation for a 2D thin cylinder

A magneto-dielectric 2D cylinder is shown in Fig. 1. The radius of the cylinder is a. The cylinder is illuminated by a normal incident plane wave TM-z or TE-z. We are interested in the calculation of its scattered far field and its dependence on the cylinder constitutive parameters. The cylinder permittivity and permeability constants are given by

$$\begin{cases} \varepsilon_1 = \varepsilon_0 \varepsilon_r = \varepsilon_0 (\varepsilon' - j\varepsilon'') & , 0 < \rho < a \\ \varepsilon_2 = \varepsilon_0 & , \rho > a \end{cases} \tag{1a}$$

$$\begin{cases} \mu_1 = \mu_0 \mu_r = \mu_0 (\mu' - j\mu'') & , 0 < \rho < a \\ \mu_2 = \mu_0 & , \rho > a \end{cases} \tag{1b}$$

The wavenumber in each medium is given by

$$\begin{cases} k_1 = k = k_0 \sqrt{\varepsilon_r \mu_r} & , 0 < \rho < a \\ k_2 = k_0 = \omega \sqrt{\varepsilon_0 \mu_0} & , \rho > a \end{cases} \tag{2}$$

In this case, the z component of the electric (TM case) and

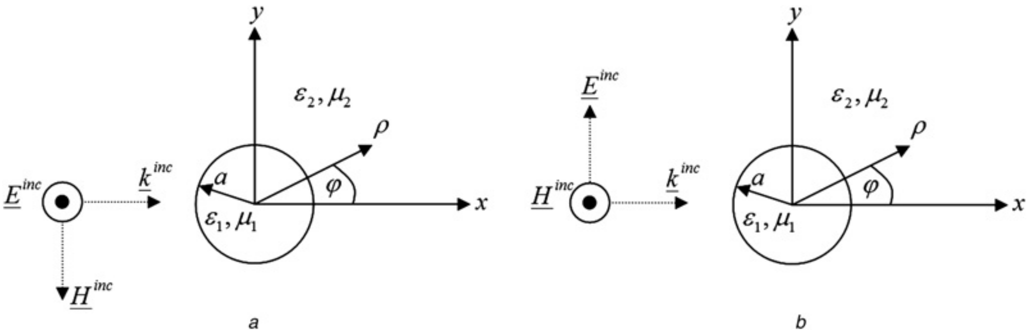

Fig. 1 *Geometry of the magneto-dielectric 2D cylinders*
a TM-z polarisation
b TE-z polarisation

magnetic (TE case) scattered far fields can be expressed in terms of cylindrical harmonics as shown in [11] by

$$E_{s,ff}^{\mathrm{TM}} \simeq -\sqrt{\frac{2j}{\pi k_0 \rho}} \mathrm{e}^{-\mathrm{j}k_0\rho} \sum_{n=-\infty}^{\infty} C_n^{\mathrm{TM}} \mathrm{e}^{\mathrm{j}n\varphi} \tag{3a}$$

$$H_{s,ff}^{\mathrm{TE}} \simeq -\sqrt{\frac{2j}{\pi k_0 \rho}} \mathrm{e}^{-\mathrm{j}k_0\rho} \sum_{n=-\infty}^{\infty} C_n^{\mathrm{TE}} \mathrm{e}^{\mathrm{j}n\varphi} \tag{3b}$$

where ρ and φ are the scattered far field cylindrical coordinates as shown in Fig. 1. The coefficients C_n^{TE} and C_n^{TM} derived in [11] are repeated here for clarity

$$C_n^{\mathrm{TM}} = \frac{\left(\sqrt{\varepsilon_r \mu_r}/\mu_r\right) J_n(k_0 a) J_n'(ka) - J_n'(k_0 a) J_n(ka)}{\left(\sqrt{\varepsilon_r \mu_r}/\mu_r\right) H_n^{(2)}(k_0 a) J_n'(ka) - H_n^{(2)'}(k_0 a) J_n(ka)} \tag{4a}$$

$$C_n^{\mathrm{TE}} = \frac{\left(\sqrt{\varepsilon_r \mu_r}/\varepsilon_r\right) J_n(k_0 a) J_n'(ka) - J_n'(k_0 a) J_n(ka)}{\left(\sqrt{\varepsilon_r \mu_r}/\varepsilon_r\right) H_n^{(2)}(k_0 a) J_n'(ka) - H_n^{(2)'}(k_0 a) J_n(ka)} \tag{4b}$$

in which $J_n(x)$ and $H_n^{(2)}(x)$ are the Bessel function and Hankel function of second type, respectively. The prime denotes derivative of the function. The terms $\left(\sqrt{\varepsilon_r \mu_r}/\mu_r\right)$ and $\left(\sqrt{\varepsilon_r \mu_r}/\varepsilon_r\right)$ are not simplified, in order to obtain the correct sign of these terms, in the cases of $\varepsilon_r < 0$ or $\mu_r < 0$. Normalisation of the fields in (3) by $-\sqrt{(2j/\pi k_0 \rho)}\mathrm{e}^{-\mathrm{j}k_0\rho}$ results in a simplified form of the scattered far fields E_s^{TM} and H_s^{TE}

$$E_s^{\mathrm{TM}} = \sum_{n=-\infty}^{\infty} C_n^{\mathrm{TM}} \mathrm{e}^{\mathrm{j}n\varphi} = C_0^{\mathrm{TM}} + 2\sum_{n=1}^{\infty} C_n^{\mathrm{TM}} \cos(n\varphi) \tag{5a}$$

$$H_s^{\mathrm{TE}} = \sum_{n=-\infty}^{\infty} C_n^{\mathrm{TE}} \mathrm{e}^{\mathrm{j}n\varphi} = C_0^{\mathrm{TE}} + 2\sum_{n=1}^{\infty} C_n^{\mathrm{TE}} \cos(n\varphi) \tag{5b}$$

For thin cylinders in terms of wavelength, we assume that $ka \ll 1$ and this infers also that $k_0 a \ll 1$. In this case, we may use small argument approximation for the Bessel and Hankel functions [12] in (4), such that

$$J_n(x) \cong \frac{1}{n!}\left(\frac{x}{2}\right)^n \ \forall \quad n \geq 1, \quad J_0(x) \cong 1$$

$$H_n^{(2)}(x) \cong j\frac{n!}{\pi n}\left(\frac{2}{x}\right)^n \ \forall \quad n \geq 1,$$

$$H_0^{(2)}(x) \cong 1 - j\frac{2}{\pi}\ln\left(\frac{\gamma x}{2}\right) \text{ with } \gamma = 1.781$$

Using the recurrence formulae of the Bessel and Hankel functions [12], it's possible to calculate the following small argument derivatives

$$J_n'(x) \cong \frac{n}{n!}\left(\frac{x}{2}\right)^n \frac{1}{x}, \quad J_0'(x) \cong -\frac{x}{2}$$

$$H_n^{(2)'}(x) \cong -j\frac{n!}{\pi x}\left(\frac{2}{x}\right)^n \text{ and } H_0^{(2)'}(x) \cong -j\frac{2}{\pi x}$$

Substitution of these small argument approximations in (4) leads for $n \geq 1$ to

$$\begin{aligned} C_n^{\mathrm{TM}} &\cong \frac{\dfrac{\sqrt{\varepsilon_r \mu_r}}{\mu_r}\dfrac{1}{ka}\dfrac{n}{n!n!}\left(\dfrac{k_0 k a^2}{4}\right)^n - \dfrac{1}{k_0 a}\dfrac{n}{n!n!}\left(\dfrac{k_0 k a^2}{4}\right)^n}{\dfrac{\sqrt{\varepsilon_r \mu_r}}{\mu_r} j\dfrac{1}{\pi k a}\left(\dfrac{k}{k_0}\right)^n + j\dfrac{1}{\pi k_0 a}\left(\dfrac{k}{k_0}\right)^n} \\ &\cong -j\pi\frac{n}{n!n!}\left(\frac{k_0^2 a^2}{4}\right)^n \frac{1-\mu_r}{1+\mu_r} \end{aligned} \tag{6a}$$

$$\begin{aligned} C_n^{\mathrm{TE}} &\cong \frac{\dfrac{\sqrt{\varepsilon_r \mu_r}}{\varepsilon_r}\dfrac{1}{ka}\dfrac{n}{n!n!}\left(\dfrac{k_0 k a^2}{4}\right)^n - \dfrac{1}{k_0 a}\dfrac{n}{n!n!}\left(\dfrac{k_0 k a^2}{4}\right)^n}{\dfrac{\sqrt{\varepsilon_r \mu_r}}{\varepsilon_r} j\dfrac{1}{\pi k a}\left(\dfrac{k}{k_0}\right)^n + j\dfrac{1}{\pi k_0 a}\left(\dfrac{k}{k_0}\right)^n} \\ &\cong -j\pi\frac{n}{n!n!}\left(\frac{k_0^2 a^2}{4}\right)^n \frac{1-\varepsilon_r}{1+\varepsilon_r} \end{aligned} \tag{6b}$$

Similarly, for $n = 0$, we obtain

$$\begin{aligned} C_0^{\mathrm{TM}} &= \frac{1-\varepsilon_r}{\left[j(2/\pi)\ln\left(\gamma k_0 a/2\right) - 1\right]\varepsilon_r + j\left(4/\pi\left(k_0 a\right)^2\right)} \\ &\cong j\frac{\left(k_0 a\right)^2 \pi}{4}\left(\varepsilon_r - 1\right) \end{aligned} \tag{7a}$$

and

$$C_0^{\mathrm{TE}} \cong j\frac{(k_0a)^2}{4}(\mu_r - 1) \tag{7b}$$

To show the convergence of the coefficients C_n^{TM} and C_n^{TE} for large n, we consider the ratios $C_{n+1}^{\mathrm{TM}}/C_n^{\mathrm{TM}}$ and $C_{n+1}^{\mathrm{TE}}/C_n^{\mathrm{TE}}$ for $n \geq 1$. Using (6), we obtain

$$\frac{C_{n+1}^{\mathrm{TM}}}{C_n^{\mathrm{TM}}} \cong \frac{-j\pi\frac{n+1}{(n+1)!(n+1)!}\left(\frac{k_0^2a^2}{4}\right)^{n+1}\frac{1-\mu_r}{1+\mu_r}}{-j\pi\frac{n}{n!n!}\left(\frac{k_0^2a^2}{4}\right)^{n}\frac{1-\mu_r}{1+\mu_r}} = \frac{(k_0a)^2}{4n(n+1)},\ n \geq 1 \tag{8a}$$

$$\frac{C_{n+1}^{\mathrm{TE}}}{C_n^{\mathrm{TE}}} \cong \frac{-j\pi\frac{n+1}{(n+1)!(n+1)!}\left(\frac{k_0^2a^2}{4}\right)^{n+1}\frac{1-\varepsilon_r}{1+\varepsilon_r}}{-j\pi\frac{n}{n!n!}\left(\frac{k_0^2a^2}{4}\right)^{n}\frac{1-\varepsilon_r}{1+\varepsilon_r}} = \frac{(k_0a)^2}{4n(n+1)},\ n \geq 1 \tag{8b}$$

As one can observe from (8a) and (8b), the coefficients C_n^{TM} and C_n^{TE} decrease rapidly as the index n increases. In Fig. 2 the ratios $\left(C_{n+1}^{\mathrm{TE}}/C_n^{\mathrm{TE}}\right)$ and $\left(C_{n+1}^{\mathrm{TM}}/C_n^{\mathrm{TM}}\right)$ are plotted for different $n \geq 1$, as a function of k_0a. One can note that $(C_2/C_1) < 10^{-3}$ for $k_0a < 0.1$ and therefore it will be sufficient to consider only the first two coefficients in the derivation. Accordingly, in the following we approximate the scattered fields for thin cylinders ($k_0a \ll 1$) in terms of only the leading terms C_0^{TM}, C_1^{TM}, C_0^{TE} and C_1^{TE}. Consequently, substitution into (5) of the approximations in (6) and (7) for C_0^{TM}, C_1^{TM}, C_0^{TE} and C_1^{TE} results in the simplified normalised scattered far fields expressions for a 2D thin cylinder

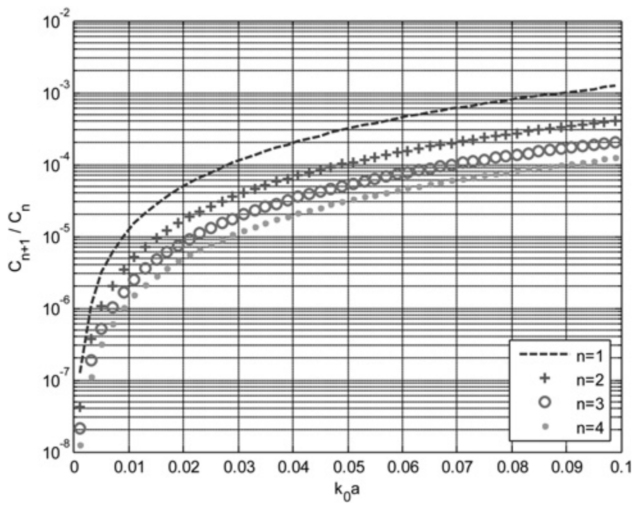

Fig. 2 *Ratio of the coefficients C_{n+1}^{TE}/C_n^{TE} as a function of k_0a*

$$E_s^{\mathrm{TM}} = K\left[\varepsilon_r - 1 - 2\frac{1-\mu_r}{1+\mu_r}\cos(\varphi)\right] \tag{9a}$$

$$H_s^{\mathrm{TE}} = K\left[\mu_r - 1 - 2\frac{1-\varepsilon_r}{1+\varepsilon_r}\cos(\varphi)\right] \tag{9b}$$

where $K = j((k_0a)^2\pi/4)$. One can observe that even though thin cylinders are considered, we still keep the dependence of the scattered far fields on the azimuth angle φ.

3 Constitutive parameters extraction from scattered far field measurements

Owing to the symmetry of the problem and without loss of generality, it is assumed that the incident angle of the illuminating field is $\varphi = 0^0$. Next, we present three extraction methods of the constitutive parameters based on the scattered far field

(a) Extraction based on the measurement of the monostatic complex scattered field for two orthogonal polarisations (TM-z and TE-z).
(b) Extraction based on the measurement of the monostatic and a bistatic complex scattered fields for one polarisation (TM-z or TE-z).
(c) Extraction based on the measurement of the monostatic radar cross section (RCS) absolute value for two orthogonal polarisations (TM-z and TE-z).

3.1 Extraction based on the measurement of the Monostatic complex scattered far field data for two orthogonal polarisations

The goal is to extract the complex permittivity and permeability of the unknown material. Substituting $\varphi = 180°$ (the monostatic case) in (9a) and (9b) leads to

$$\frac{E_s^{\mathrm{TM}}(180°)}{K} = \varepsilon_r - 1 + 2\frac{1-\mu_r}{1+\mu_r} \tag{10a}$$

$$\frac{H_s^{\mathrm{TE}}(180°)}{K} = \mu_r - 1 + 2\frac{1-\varepsilon_r}{1+\varepsilon_r} \tag{10b}$$

Extraction of ε_r from (10a) results into

$$\varepsilon_r = \varepsilon' - j\varepsilon'' = \frac{E_s^{\mathrm{TM}}(180°)}{K} + 1 - 2\frac{1-\mu_r}{1+\mu_r} \tag{11}$$

Back substitution of (11) into (10b) results into a quadratic equation of μ_r, such that

$$\mu_r^2 - \mu_r B + C = 0 \tag{12}$$

where

$$B = B_R + jB_I \triangleq -\left(\frac{H_s^{\mathrm{TE}}(180°)}{K} + 2\right) \tag{13}$$

and

$$C = C_R + jC_I \triangleq \frac{4 - 3\left(E_s^{\mathrm{TM}}(180^\circ)/K\right) - \left(\left(E_s^{\mathrm{TM}}(180^\circ)H_s^{\mathrm{TE}}(180^\circ)\right)/K^2\right)}{\left(E_s^{\mathrm{TM}}(180^\circ)/K\right) + 4} \quad (14)$$

Substitution of $\mu_r = \mu' - j\mu''$ in (12) and separation of the real and imaginary parts leads to

$$(\mu')^2 - (\mu'')^2 + B_R\mu' + B_I\mu'' + C_R = 0 \quad (15a)$$

$$-2\mu'\mu'' - B_R\mu'' + B_I\mu' + C_I = 0 \quad (15b)$$

Equations (15a) and (15b) can be rearranged in the following short form

$$\frac{\left(\mu' + (B_R/2)\right)^2}{(1/4)\left(B_R^2 - B_I^2\right) - C_R} - \frac{\left(\mu'' - (B_I/2)\right)^2}{(1/4)\left(B_R^2 - B_I^2\right) - C_R} = 1 \quad (16a)$$

$$\mu'' = \frac{B_I\mu' + C_I}{2\mu' + B_R} \quad (16b)$$

Equation (16a) describes an hyperbola in the complex μ-plane with the origin at $(\mu' = -(B_R/2),\ \mu'' = (B_I/2))$. The graphical interpretation of the sign of $(1/4)\left(B_R^2 - B_I^2\right) - C_R$ is the rotation of the hyperbola in the μ-plane by 90°. Moreover, (16b) has two asymptotes: a vertical one ($\mu'' \to \infty$) at the singular point $\mu' = -(B_R/2)$ and a horizontal one ($\mu' \to \infty$) at $\mu'' = (B_I/2)$. The intersection of the two functions in (16) determines the the solutions of μ_r. Given μ_r, the permittivity ε_r can be computed through (11).

Fig. 3 shows a graphical representation of equations (16a) and (16b) for a typical cylinder with radius $a = 0.5$ mm at 3 GHz. The scattering fields used for the parameters extraction were computed by the finite element method (FEM) commercial software HFSS from ANSYS. The cylinder parameters used for this simulation were: $\varepsilon_r = 2.0 - j1.0$, $\mu_r = 3 - j3.5$ Inspection of the plots in Fig. 3 reveal two solutions for μ_r, which is a clear indication of the ambiguity in the solution. The correct solution based on physical considerations is that with $\mu'' > 0$. In case that both solutions satisfy this condition on μ'', we may need to resort to scattering data from another azimuth angle φ to resolve the ambiguity as explained in the next section.

For validation purposes of the approximations made in the analytical computation of the scattered fields, a comparison was made between the TM and TE polarised scattering patterns of the cylinder computed through the analytical representation (5) with thirty elements in the summation, the approximated analytical representation for thin cylinders ($ka < 0.1$) (9) with only two elements in the summation and the scattering pattern computed using HFSS. Fig. 4 shows the cylinder geometry used for the HFSS simulation. To obtain in HFSS simulations the effect of an infinite cylinder, Master and Slave periodic structure boundary conditions were used in z direction for a cylinder with a length h. In addition, the scattered far field simulated by HFSS for a three-dimensional (3D) cylindrical scatter with a length h was converted to the scattered far field for a 2D scatter through the relationship $E_s^{3D} \simeq E_s^{2D}\left(he^{j\pi/4}/\sqrt{\lambda_0\rho}\right)|_{\rho=r}$ [13]. This conversion is necessary to compare the HFSS results to the fields computed through (5) and (9). The circular cylinder was embedded in free space and surrounded by a perfect matching layer to avoid spurious reflections in the simulations as shown in Fig. 4. Fig. 5 shows a typical comparison between the scattering patterns (analytical-30 terms, analytical-2 terms and numerical HFSS) of a cylinder with parameters: $a = 0.5$ mm ($|ka| = 0.1$), $\varepsilon_r = 2.0 - j1.0$, $\mu_r = 3 - j3.5$ at $f = 3$ GHz and

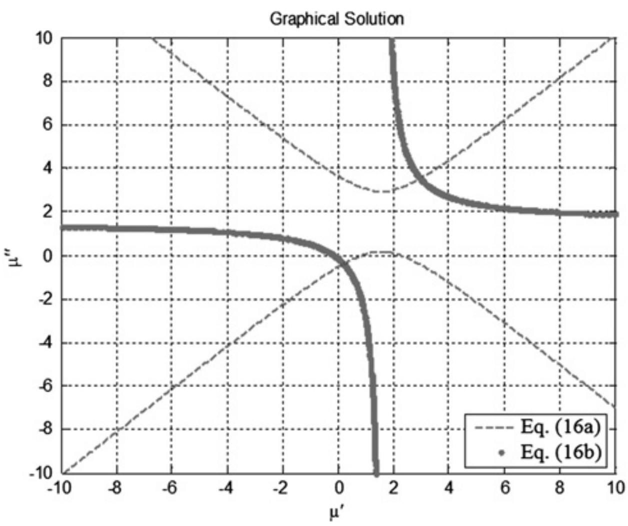

Fig. 3 *Graphical solution for method 1- complex monostatic measurements for two polarizations, $f = 3$ GHz, $a = 0.5$ mm, $\varepsilon_r = 2.0 - j1.0$, $\mu_r = 3 - j3.5$*

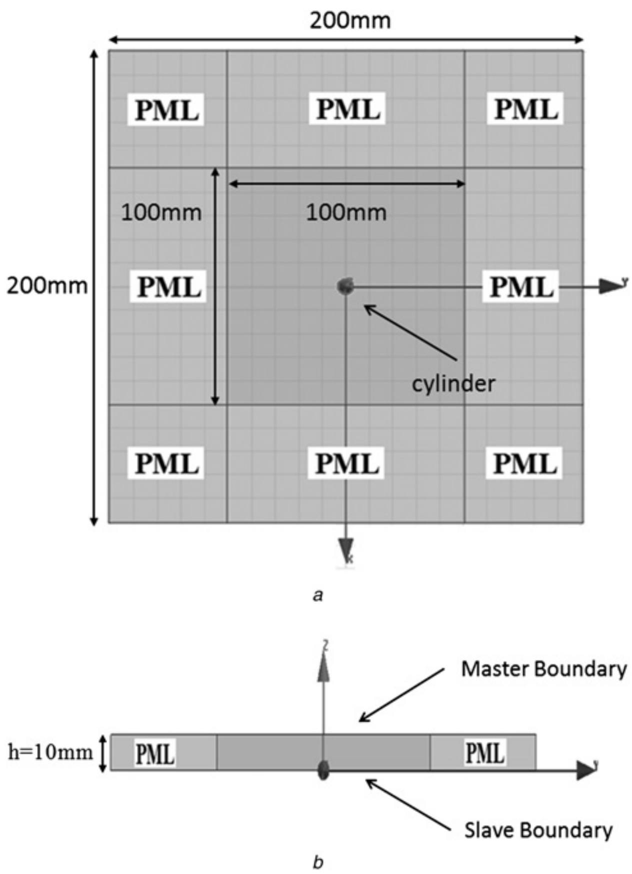

Fig. 4 *Simulation setup for the FEM calculation using HFSS*

a Top View
b Side View

doi: 10.1049/iet-map.2013.0714

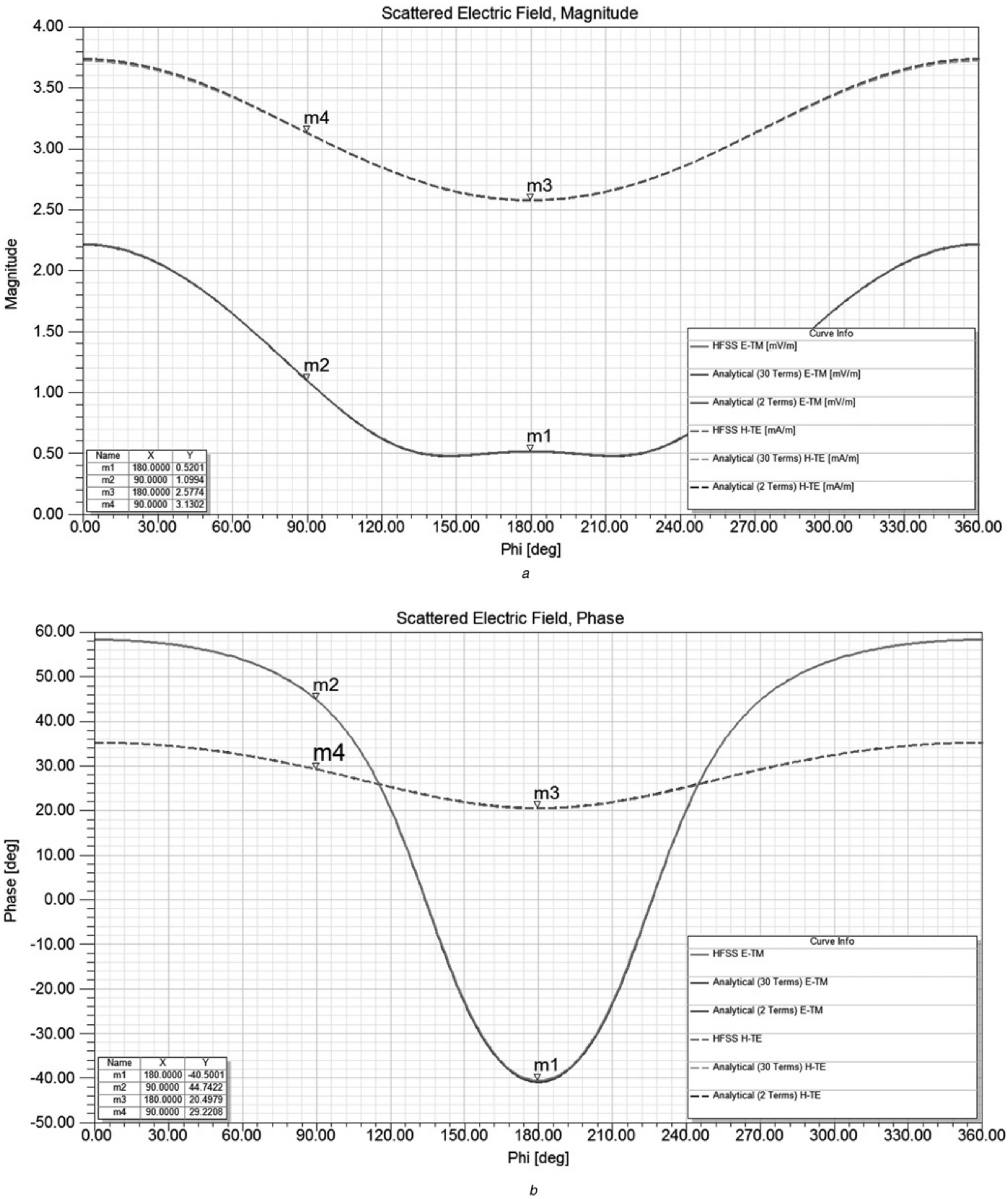

Fig. 5 *Comparison of complex bistatic scattering patterns simulations (analytical, analytical approximation for thin cylinders, numerical with HFSS) for two polarisations TE and TM, f = 3 GHz, a = 0.5 mm, $\varepsilon_r = 2.0 - j1.0$, $\mu_r = 3 - j3.5$*

a Magnitude
b Phase

two orthogonal polarisations. One can observe a very good agreement between the patterns, which justifies the approximations made for thin cylinders.

Next, we present two examples and compute the constitutive parameters of the cylinders based on the scattering data simulated with HFSS. We use the simulation with HFSS as an alternative to measured data.

Example 1: Initially, we compute the scattered fields with HFSS for a cylinder with $\varepsilon_r = 2.0 - j1.0$, $\mu_r = 3.0 - j3.5$,

$a = 0.5$ mm at the frequency $f = 3$ GHz ($|ka| = 0.1$). The scattering fields computed with HFSS used as alternative to measured data are shown in Fig. 5

$$E_s^{\mathrm{TM}}(180^\circ) = 0.52\angle - 40.5^\circ \left[\frac{\mathrm{mV}}{\mathrm{m}}\right]$$

$$\text{and } H_s^{\mathrm{TE}}(180^\circ) = 2.58\angle 20.5^\circ \left[\frac{\mathrm{mA}}{\mathrm{m}}\right]$$

Using (12) to compute $\mu_r = \mu' - j\mu''$, we obtain two solutions $\mu_{r1} = 2.967 - j3.518$ and $\mu_{r2} = 0.198 + j0.404$. μ_{r2} is a non-physical solution since $\mu''_{r2} < 0$. Using (11) with μ_{r1}, we obtain $\varepsilon_r = 1.999 - j1.011$. We can note a good agreement in the extracted parameters.

Example 2: In this example we consider a material without losses. Assume, $f = 3$ GHz, $\varepsilon_r = -2$, $\mu_r = -3$, $a = 0.5$ mm ($|ka| = 0.077$). The scattering fields computed with HFSS are

$$E_s^{\mathrm{TM}}(180^\circ) = 5.40\angle - 89.98^\circ \left[\frac{\mathrm{mV}}{\mathrm{m}}\right]$$

$$\text{and } H_s^{\mathrm{TE}}(180^\circ) = 7.77\angle - 89.99^\circ \left[\frac{\mathrm{mA}}{\mathrm{m}}\right]$$

Using (12), we obtain two values of the cylinder permeability $\mu_{r1} = -5.003$ and $\mu_{r2} = -3.033$. These results mean that we have ambiguity and to resolve it we need another scattered field measurement at a different azimuth angle. The required procedure for this case is explained in the next section.

3.2 Extraction based on the measurement of a monostatic and a bistatic complex scattered field data for one polarisation

This method is derived for TM-z polarisation but is similar for TE-z polarisation. Without loss of generality, we consider for simplicity the scattered field at $\varphi = 90°$. In this case (9a) can be rewritten in the form

$$\frac{E_s^{\mathrm{TM}}(90^\circ)}{K} = \varepsilon_r - 1 \tag{17}$$

Solving (17) for ε_r leads to

$$\varepsilon_r = \frac{E_s^{\mathrm{TM}}(90^\circ)}{K} + 1 \tag{18a}$$

Next, based on (10a), we can express the permeability μ_r in terms of the monostatic scattered electric field ($\varphi = 180°$) by

$$\mu_r = \frac{1 - (1/2)\left[\left(E_s^{\mathrm{TM}}(180^\circ)/K\right) - \varepsilon_r + 1\right]}{1 + (1/2)\left[\left(E_s^{\mathrm{TM}}(180^\circ)/K\right) - \varepsilon_r + 1\right]} \tag{18b}$$

For validation purpose we have considered the previous examples,

Example 3: Instead of measurements, we use simulated scattered fields with HFSS at $\varphi = 90°$ and $\varphi = 180°$ for a cylinder with $a = 0.5$ mm($|ka| = 0.1$), $\varepsilon_r = 2.0 - j1.0$, $\mu_r = 3.0 - j3.5$ at $f = 3$ GHz. The bistatic and monostatic scattered fields computed with HFSS and shown in Fig. 5 are,

$$E_s^{\mathrm{TM}}(180^\circ) = 0.52\angle - 40.50^\circ \left[\frac{\mathrm{mV}}{\mathrm{m}}\right]$$

$$\text{and } E_s^{\mathrm{TM}}(90^\circ) = 1.09\angle 44.74^\circ \left[\frac{\mathrm{mV}}{\mathrm{m}}\right]$$

Using (18), we obtain the extracted values of $\varepsilon_r = 1.999 - j1.007$ and $\mu_r = 2.989 - j3.505$, which is in a very good agreement with the initial parameters.

Example 4: The HFSS simulated scattered fields at $\varphi = 90°$ and $\varphi = 180°$ for a cylinder with parameters: $a = 0.5$ mm, ($|ka| = 0.077$), $\varepsilon_r = -2$, $\mu_r = -3$ at $f = 3$ GHz are

$$E_s^{\mathrm{TM}}(180^\circ) = 5.40\angle - 89.98^\circ \left[\frac{\mathrm{mV}}{\mathrm{m}}\right]$$

$$\text{and } E_s^{\mathrm{TM}}(90^\circ) = 2.31\angle - 89.85^\circ \left[\frac{\mathrm{mV}}{\mathrm{m}}\right]$$

Using (18), we obtain $\varepsilon_r = -1.989 - j0.008$ and $\mu_r = -3.023 - j0.006$. One can recognise a good agreement in the parameter extraction.

As noted from these examples, using the second method the correct solution is obtained without any ambiguity. The drawback of this method lies in the requirement for a bistatic measurement, which its set-up is more complex for implementation.

3.3 Extraction based on the measurement of the monostatic RCS absolute value for two polarisations

Using this method the following assumptions are made:

1. The material is lossy dielectric and isotropic.
2. The extraction is based on the measured RCS monostatic $\sigma_{\mathrm{TM,TE}}(180°)$ absolute values.

In the derivation for practical reasons, the TM or TE RCS, $\sigma_{\mathrm{TM,TE}}(\varphi)$ were used instead of the corresponding scattered fields. Based on [11] the bistatic RCS for TM and TE polarisations can be expressed in terms of cylindrical harmonics by

$$\sigma_{\mathrm{TM}}(\varphi) = \frac{4}{k_0}\left|C_0^{\mathrm{TM}} + 2\sum_{n=1}^{\infty} C_n^{\mathrm{TM}} \cos(n\varphi)\right|^2 \tag{19a}$$

$$\sigma_{\mathrm{TE}}(\varphi) = \frac{4}{k_0}\left|C_0^{\mathrm{TE}} + 2\sum_{n=1}^{\infty} C_n^{\mathrm{TE}} \cos(n\varphi)\right|^2 \tag{19b}$$

where the coefficients $C_n^{\mathrm{TE,TM}}$ are given in (6) and (7) for thin cylinders. We start with the case of a thin lossy dielectric cylinder ($\varepsilon_r = \varepsilon' - j\varepsilon''$, $\mu_r = 1$) and consider based on the discussion in chapter 2 only the first two coefficients to compute $\sigma_{\mathrm{TM,TE}}(\varphi)$. Substitution of these coefficients in (19) results in approximated expressions for the TM and TE

doi: 10.1049/iet-map.2013.0714

monostatic RCS

$$\sigma_{\mathrm{TM}}\left(180^{\circ}\right) \cong \frac{\pi^{2}\left(k_{0} a\right)^{4}}{4 k_{0}}\left[\left(\varepsilon^{\prime}-1\right)^{2}+\left(\varepsilon^{\prime \prime}\right)^{2}\right] \tag{20a}$$

$$\sigma_{\mathrm{TE}}\left(180^{\circ}\right) \cong \frac{\pi^{2}\left(k_{0} a\right)^{4}}{k_{0}} \frac{\left(\varepsilon^{\prime}-1\right)^{2}+\left(\varepsilon^{\prime \prime}\right)^{2}}{\left(\varepsilon^{\prime}+1\right)^{2}+\left(\varepsilon^{\prime \prime}\right)^{2}} \tag{20b}$$

Extracting $(\varepsilon'')^2$ from (20a) and (20b) yields

$$\left(\varepsilon^{\prime \prime}\right)^{2}=\frac{4 k_{0} \sigma_{TM}\left(180^{\circ}\right)}{\pi^{2}\left(k_{0} a\right)^{4}}-\left(\varepsilon^{\prime}-1\right)^{2} \tag{21a}$$

$$\left(\varepsilon^{\prime \prime}\right)^{2}=\frac{\left(\varepsilon^{\prime}-1\right)^{2}-\left(\varepsilon^{\prime}+1\right)^{2}\left(k_{0} \sigma_{\mathrm{TE}}\left(180^{\circ}\right) / \pi^{2}\left(k_{0} a\right)^{4}\right)}{k_{0} \sigma_{\mathrm{TE}}\left(180^{\circ}\right) / \pi^{2}\left(k_{0} a\right)^{4}-1} \tag{21b}$$

Comparison of (21a) and (21b) leads to

$$\varepsilon^{\prime}=\frac{\sigma_{\mathrm{TM}}\left(180^{\circ}\right)\left(1-\sigma_{\mathrm{TE}}\left(180^{\circ}\right)\left(k_{0} / \pi^{2}\left(k_{0} a\right)^{4}\right)\right)}{\sigma_{\mathrm{TE}}\left(180^{\circ}\right)} \tag{22}$$

Given ε' in (22), one can evaluate ε'' by back substitution into (21a) to obtain

$$\varepsilon^{\prime \prime}=\sqrt{\frac{4 \sigma_{\mathrm{TM}}\left(180^{\circ}\right)}{k_{0}^{3} a^{4} \pi^{2}}-\left(\varepsilon^{\prime}-1\right)^{2}} \tag{23}$$

Expressions (22) and (23) give the complex dielectric constant of the thin cylinder in terms of two orthogonal polarisations monostatic RCS measurement values. In case of multiple solutions, note that from physical considerations ε'' should be positive as a follow-up of the complex dielectric constant definition $\varepsilon_r = \varepsilon' - j\varepsilon''$.

An alternative graphical solution can be obtained if one recognises that (21a) and (21b) can be rewritten in the form

$$\left(\varepsilon^{\prime \prime}\right)^{2}+\left(\varepsilon^{\prime}-1\right)^{2}=\frac{4 k_{0} \sigma_{\mathrm{TM}}\left(180^{\circ}\right)}{\pi^{2}\left(k_{0} a\right)^{4}} \tag{24a}$$

$$\left(\varepsilon^{\prime \prime}\right)^{2}+\left[\varepsilon^{\prime}+\frac{\sigma_{\mathrm{TE}}\left(180^{\circ}\right)+k_{0}^{3} a^{4} \pi^{2}}{\sigma_{\mathrm{TE}}\left(180^{\circ}\right)-k_{0}^{3} a^{4} \pi^{2}}\right]^{2} =\frac{4 \pi^{2}\left(k_{0} a\right)^{4} \sigma_{\mathrm{TE}}\left(180^{\circ}\right) k_{0}}{\left[\sigma_{\mathrm{TE}}\left(180^{\circ}\right) k_{0}-\pi^{2}\left(k_{0} a\right)^{4}\right]^{2}} \tag{24b}$$

Equation (24a) describes a circle in the complex ε-plane with the centre at $(\varepsilon' = 1,\ \varepsilon'' = 0)$ and with a radius $\left(2\sqrt{k_0\sigma_{TM}(180^\circ)}/\pi(k_0a)^2\right)$, whereas (24b) describes a circle with the centre at

$$\left(\varepsilon^{\prime}=-\frac{\sigma_{\mathrm{TE}}\left(180^{\circ}\right)+k_{0}^{3} a^{4} \pi^{2}}{\sigma_{\mathrm{TE}}\left(180^{\circ}\right)-k_{0}^{3} a^{4} \pi^{2}}, \varepsilon^{\prime \prime}=0\right)$$

and with a radius

$$\frac{2 \pi\left(k_{0} a\right)^{2} \sqrt{\sigma_{\mathrm{TE}}\left(180^{\circ}\right) k_{0}}}{\left|\sigma_{\mathrm{TE}}\left(180^{\circ}\right) k_{0}-\pi^{2}\left(k_{0} a\right)^{4}\right|}$$

The intersection of the two functions in (24) determines the graphical solutions of ε_r. Fig. 6 shows a graphical representation of (24a) and (24b) for a typical cylinder with radius $a = 0.5$ mm at 3 GHz. The RCS used for the parameters extraction were computed using HFSS instead of using measured data. The cylinder parameters used for this simulation were: $\varepsilon_r = 2.0 - j1.5$, $\mu_r = 1$. Inspection of the plots in Fig. 6 reveals two solutions for ε_r, which is an indication of the ambiguity in the solution. The correct solution based on physical considerations is that with $\varepsilon'' > 0$.

Next for validation purpose, two examples have been considered

Example 5: Initially the monostatic RCS for TE and TM polarisations have been simulated using HFSS for a cylinder with a height $h = 10$ mm in z direction, which was extended to an infinite long cylinder using the Master/Slave boundary conditions as shown in Fig. 4. The conversion of the RCS from a 3D scatter obtained through HFSS to the RCS of a 2D scatter with the same cross section was obtained using the relationship $\sigma^{3D} \simeq \sigma^{2D}\left(2h^2/\lambda_0\right)$ [13]. The cylinder parameters are: $a = 0.5$ mm ($|ka| = 0.05$), $\varepsilon_r = 2.0 - j1.5$, $\mu_r = 1$ at $f = 3$ GHz. This data have been used instead of measured data. The simulated RCS results using HFSS are: $10\log[\sigma_{\mathrm{TM}}(180^0)/\lambda] = -59.04$ dB and $10\log[\sigma_{\mathrm{TE}}(180^0)/\lambda] = -63.51$ dB. Substitution of these RCS values in (22) and (23) results in $\varepsilon_r = 1.984 - j1.514$. One can recognize a good agreement in the extracted parameters.

Example 6: In this example a thin cylinder with lossy negative dielectric constant and $a = 0.5$ mmat $f = 3$ GHz was considered. The simulated RCS with HFSS for a dielectric

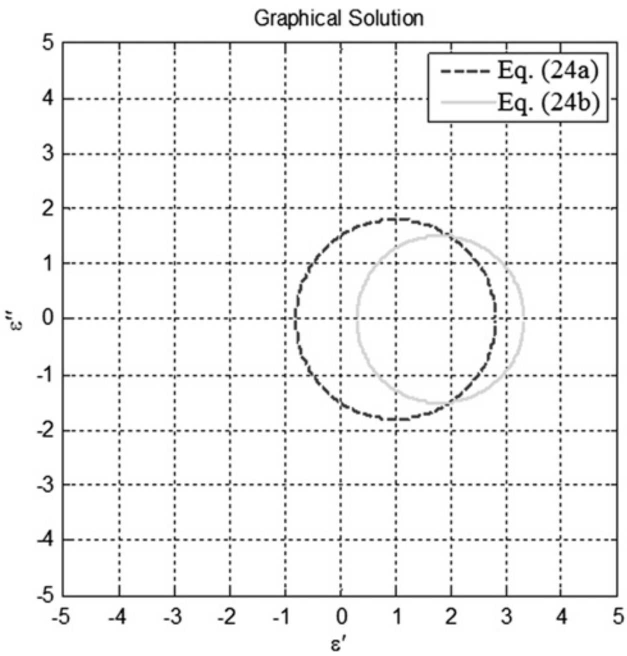

Fig. 6 *Graphical solution for method 3 using absolute monostatic RCS measurement for two polarisations, $f = 3$ GHz, $a = 0.5$ mm, $\varepsilon_r = 2.0 - j1.5$, $\mu_r = 1$*

constant $\varepsilon_r = -2.0 - j1.5$ are $10\log[\sigma_{TM}(180°)/\lambda] = -53.68$ dB and $10\log[\sigma_{TE}(180°)/\lambda] = -52.69$ dB. Substitution of this data in (22), (23) results in $\varepsilon_r = -2.004 - j1.475$. The extracted constitutive parameters are in a good agreement with the initial parameters.

In a similar fashion, it is possible to derive a method in order to extract the constitutive parameters of a magnetic 2D isotropic cylinder with losses.

4 Conclusions

Three methods for extracting the constitutive parameters of thin cylinders based on the measurement of the scattered fields have been presented.

In the first method, we propose to extract both complex permittivity and permeability of the 2D magneto-dielectric thin cylinder using the monostatic complex scattered fields for both polarisations (TM-z and TE-z). Using this method, we may encounter ambiguity of the constitutive parameters, and need more azimuth scattered far field measurements in order to resolve it. This brings us to the second method.

In the second method, the complex scattered far field measurements are carried out for one polarisation, but for two azimuth angles, which makes the process more complicated. In this method there is no ambiguity and it is possible to obtain both complex constitutive parameters.

In the third method, we propose to extract the complex permittivity or the complex permeability by measuring only the absolute value of the monostatic RCS for both polarisations. This is the easiest method for practical implementation, since its experimental set-up is the simplest including the calibration process. The drawback of this method is that it does not enable to extract all constitutive parameters and it evaluates either the complex permittivity or the complex permeability.

5 References

1 Chen, L., Ong, C., Neo, C., Varadan, V.K., Varadan, V.K.: 'Microwave electronics: measurement and materials characterization' (Wiley, 2004)

2 Stuchly, M., Athey, T., Taylor, G.: 'Measurements of radio frequency permittivity of biological tissues with an open - ended coaxial line: Part 2 experimental results', *IEEE Trans. Microw. Theory Tech.*, 1982, **30**, (2), pp. 192–198

3 Huang, Y.: 'Design, calibration and data interpretation for a one port large coaxial dielectric measurement cell', *Meas. Sci. Technol.*, 2001, **12**, (1), pp. 111–115

4 Boughriet, A., Legrand, A., Chapoton, A.: 'Non-iterative stable transmission/reflection method for low loss material complex permittivity determination', *IEEE Trans. Microw. Theory Tech.*, 1997, **45**, (1), pp. 52–57

5 Esterban, H., Catala-Civera, J., Cogollos, S., Boria, V.: 'Characterization of complex permittivity properties of materials in rectangular waveguides using a hybrid iterative method', *IEEE Microw. Guid. Wave Lett.*, 1997, **10**, (5), pp. 186–188

6 Ghodgaonkar, D., Varadan, V.V., Varadan, V.K.: 'Free-space measurements of complex permittivity and complex permeability of magnetic materials at microwave frequencies', *IEEE Trans. Instrum. Meas.*, 1990, **39**, pp. 387–394

7 Damaskos, N.: 'Measuring dielectric constants of low loss materials using a broadband cavity technique', *Microw. J.*, 1995, **38**, (9), pp. 140–149

8 Kent, G.: 'Dielectric resonances for measuring dielectric properties', *Microw. J.*, 1988, **31**, (10), pp. 90–114

9 Lynch, A.: 'Measurement of dielectric properties in an open resonator'. Proc. IEE Conf. on Dielectric Materials Measurements and Applications, Institute of Electrical Engineers, London, 1979, vol. 177, pp. 373–376

10 Kobayashi, Y., Katoh, M.: 'Microwave measurement of dielectric properties of low loss materials by the dielectric rod resonator method', *IEEE Trans. Microw. Theory Tech.*, 1985, **33**, (7), pp. 586–592

11 Bussey, H., Richmond, J.: 'Scattering by a lossy dielectric circular cylindrical multilayer, numerical values', *IEEE Trans. Antennas Propag.*, 1975, **23**, (5), pp. 723–725

12 Lipschutz, S., Murray, S., Liu, J.: 'Schaum's Outline of Mathematical Handbook of Formulas and Tables', Ed. 4th, Schaum's Outline Series

13 Balanis, C.A.: 'Advanced engineering electromagnetics' (Wiley, New York, 1989), ch. 11

IET Microw. Antennas Propag., 2015, Vol. 9, Iss. 6, pp. 585–592
doi: 10.1049/iet-map.2013.0714